ACS APPLIED MATERIALS & INTERFACES

Research Article

www.acsami.org

Energetics and Kinetics of Li Intercalation in Irradiated Graphene Scaffolds

J. Song* and B. Ouyang

Department of Mining and Materials Engineering, McGill University, Montreal, Quebec, Canada

N. V. Medhekar*

Department of Materials Engineering, Monash University, Clayton, Victoria, Australia

Supporting Information

ABSTRACT: In the present study, we investigate the irradiation-defects hybridized graphene scaffold as one potential building material for the anode of Li-ion batteries. Designating the Wigner V_2^2 defect as a representative, we illustrate the interplay of Li atoms with the irradiation defects in graphene scaffolds. We examine the adsorption energetics and diffusion kinetics of Li in the vicinity of a Wigner V_2^2 defect using density functional theory calculations. The equilibrium Li adsorption sites at the defect are identified and shown to be energetically preferable to the adsorption sites on pristine (bilayer) graphene. Meanwhile, the minimum energy paths and corresponding energy barriers for Li migration at the defect are determined and computed. We find that, while the defect is shown to exhibit certain trapping effects on Li motions on the graphene surface, it appears to facilitate the interlayer Li diffusion and enhance the charge capacity within its vicinity, because of the reduced interlayer spacing and characteristic symmetry associated with the defect. Our results provide critical assessment for the application of irradiated graphene scaffolds in Li-ion batteries.

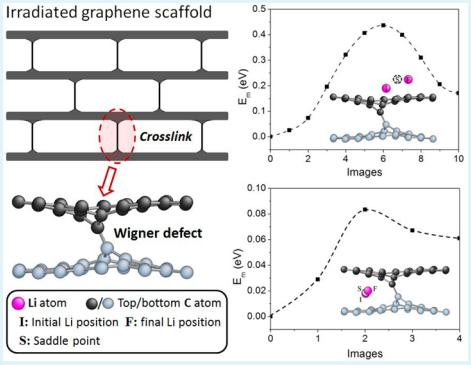

KEYWORDS: *irradiation-induced defect, graphene scaffold, Li-ion battery, diffusion kinetics, density functional theory*

INTRODUCTION

Carbon-based materials such as graphite and multilayer graphene have drawn paramount interest as a state-of-art anode material for Li-ion batteries.[1−5] These materials exhibit good Li storage capacity and fast charge/discharge characteristics.[6−10] They also possess high electronic/thermal conductivity and fast Li diffusion, which are especially advantageous for battery applications.[11−13] In addition, they exhibit excellent in-plane mechanical integrity and are often combined with other high-capacity anode materials (Si, $FePO_4$, etc.)[14−16] to improve the failure resistance and cycling performance of Li-ion batteries.

One major challenge associated with intercalation based Li-ion batteries is the repeated volume expansion/shrinkage during Li insertion/extraction. The volume change can be substantial (i.e., >150%) for high-capacity Li-ion batteries,[17,18] leading to substantial stress that causes electrode fracture, loss of electrical contact, and rapid fading of capacity. Graphite/multilayer graphene, despite their in-plane strength, are also vulnerable to large volumetric deformations, because of the weak bonding (van der Waals forces) between graphene sheets, and often suffer interlayer failure during Li intercalation. For instance, one major cause of degradation in graphite-based Li-ion batteries is the constant breakage and reformation of the solid electrolyte interfaces,[19,20] due to exfoliation.[21,22]

However, the above challenges pertinent to graphite/multilayer graphene may be potentially overcome by fabricating hybrid three-dimensional (3D) graphene scaffolding structures where graphene sheets are "cross-linked" through covalent bonds between neighboring sheets, as illustrated in Figure 1a. The idea of such scaffolding structures has been previously demonstrated by da Silva et al.[23] for carbon nanotube bundles (CNBs) where covalent bonds form strong crosslinks between individual nanotubes, leading to a sizable increase in the shear modulus of CNBs. It has been shown[23−28] that the covalent crosslinks in carbon-based materials can be introduced via high-energy defects produced by irradiation.[29−31] In particular, for graphite/multilayer graphene, one prevailing category of such defects are the Wigner defects.[32] The Wigner defects exhibit formation energies and migration barriers on the order of ∼10 eV, making them thermodynamically stable and immobile at ambient temperature. However, the presence of those defects necessarily modifies the local atomic and electronic structures, and, subsequently, how Li atoms interact with graphite/multilayer graphene. In this regard, it is of great importance to understand the interactions between Li atoms and the Wigner

Received: August 29, 2013
Accepted: November 20, 2013
Published: November 20, 2013

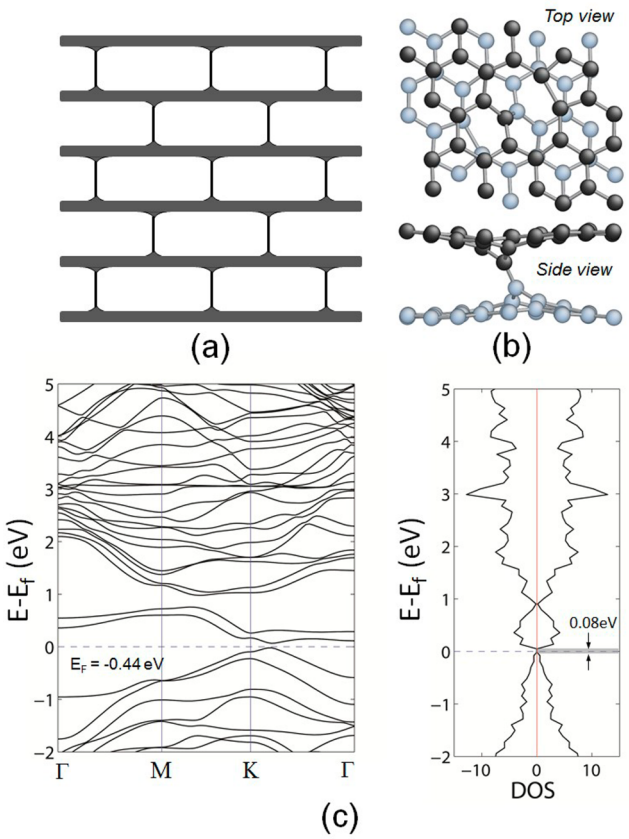

Figure 1. (a) Illustration of an example 3D graphene scaffold structure, where neighboring graphene sheets (i.e., colored dark gray) are bridged through covalent links (i.e., indicated by vertical line segments) provided by cross-planar defects. (b) Top and side projection views of the Wigner V_2^2 defect, with the C atoms in different graphene sheets colored dark gray and cyan for clarity. The corresponding band structure and density of states (DOS) plots of the system are shown in panel (c), where a band gap opening of 0.08 eV is indicated.

defects, and how their interactions impact the Li transport process and, consequently, battery performance.

In the present study, we focus on a AB-stacked bilayer graphene with a Wigner V_2^2 defect[23] as a simple version of the graphene scaffold to illustrate the role of irradiation defects during Li intercalation. Through density functional theory (DFT) calculations, the equilibrium adsorption sites and energetics of Li atoms, in the low concentration limit, in the vicinity of the defect are identified. Meanwhile the charge transfer processes and electronic structures for various Li-defect configurations are investigated. The local migration paths/barriers of Li at the defect then are examined. In the end, the implications of our findings on Li transport in irradiated graphene scaffolds and, subsequently, the charging behaviors of Li-ion batteries are discussed.

1. COMPUTATIONAL METHODOLOGY

Spin-polarized density functional theory (DFT) calculations were performed using the Vienna ab initio Simulation Package (VASP)[33] with projector augmented-wave (PAW) potentials.[34,35] The electrons explicitly included in the calculations are the ($2s^2 2p^2$) electrons of C and the ($1s^2 2s^1$) electrons of Li. A cutoff energy of the plane wave basis set of 800 eV is used in all calculations. The Wigner V_2^2 defect examined in this study is a crossplanar divacancy formed as a result of the coalescence of two interplanar vacancies. It exhibits lower formation energy and thus thermodynamically more stable than other Wigner divacancy defects. Nonetheless, preliminary studies on the other Wigner divacancy defects (e.g., Wigner V_2^1) have also been performed, showing largely similar results (i.e., in terms of Li energetics and kinetics at the defect).

In all calculations, a simulation cell with a Wigner V_2^2 defect centered in a $4 \times 4 \times 1$ bilayer graphene is created, as shown in Figure 1. Sample calculations using larger cell sizes (i.e., up to $8 \times 8 \times 1$ cell) are also performed, showing no size dependence of our results. The distance between two neighboring bilayer graphenes is chosen to be 15 Å to eliminate image interactions across the periodic boundary perpendicular to the graphene sheet. The simulation cell is first relaxed with both the cell shape and volume allowed to change to reach the ground state, following which Li atoms are introduced individually to examine their adsorption at the defect. In the relaxations of ionic coordinates and supercell vectors, the convergence was considered reached when the forces on all ions were less than 0.01 eV/Å. The migration kinetics of Li between neighboring adsorption sites then are investigated using the climbing image Nudged Elastic Band (ci-NEB) method.[36] The NEB calculation is considered converged when the force on each image is less than 0.01 eV/Å.

One thing to note is that the van der Waals (vdW) interactions were not considered in the present study. Previously, it was shown by Lee et al.[37] and Fan et al.[38] that the vdW interactions can have sizable effects on the Li adsorption energy on graphene. However, we find that the vdW interactions have rather small influence on Li adsorption around the Wigner defect (see the Supporting Information). This is likely due to the interlayer bond at the defect. The interlayer bond, being covalent in nature, dominates the local atomic structure at the defect and thus the Li energetics.

2. RESULTS AND DISCUSSION

2.1. Benchmark Results of the Wigner V_2^2 Defect. To put the interplay between the Wigner V_2^2 defect and Li atoms into proper perspective, we first examine the structural and electronic properties of the Wigner defect in the absence of Li. The relaxed atomic configuration of the defect is shown in Figure 1b. The graphene sheets at the defect are interconnected via a covalent bond of 1.38 Å in length. C atoms reconstruct at the vicinity of the defect, exhibiting considerable out-of-plane displacements. These results are in excellent agreement with those previously reported in ref 32.

The significant geometric reconstruction induced by the defect necessarily modifies the local electronic properties. In this regard, we examine the band structure and density of states (DOS) of the system, shown in Figure 1c. We note from Figure 1c that the system exhibits a Fermi energy of $E_f = -0.438$ eV, which is ~0.08 eV lower than the pristine bilayer graphene. Also, we see that there is a noticeable band gap of $\Delta E \approx 0.08$ eV[39] at the Fermi level, in comparison to the near-zero band gap in the pristine bilayer graphene. Analysis of the DOS shows that the bands near the Fermi level come from those reconstructed C atoms in the immediate vicinity of the defect, suggesting that the band gap (or doping level in the case of dilute defect concentration; see note in ref 39) directly attributes to the Wigner defect.

2.2. Energetics and Electronic Structures of Li Atoms at a Wigner V_2^2 Defect. Li atoms, when intercalated into a AB-stacked bilayer graphene (with or without the Wigner V_2^2 defect), may either occupy sites on the outer surfaces or between two graphene layers, denoted as T-sites and M-sites, respectively. We note that the locations of these sites can be different as the Li concentration varies.[40] For the sake of simplicity, in the context below, we limit our discussion to the low Li concentration regime.

For a pristine AB-stacked bilayer graphene, the Li adsorption on the outer surfaces is similar to the case of a monolayer graphene, with the equilibrium T-sites being directly on top of the hexagon (hollow sites), instead of on top of C atoms (i.e., top sites) or on top of C−C bonds; while the equilibrium M-sites are hollow sites with respect to one graphene sheet and top sites with respect to the other graphene sheet.[28,41,42] To assess the energetics of Li adsorption on bilayer graphene, we compute the adsorption energy of a Li adatom (E_{ad}) as

$$E_{ad} = E_{Li\text{-}GP} - E_{Li} - E_{GP} \quad (1)$$

where $E_{Li\text{-}GP}$, E_{Li}, and E_{GP} denote the total energy of Li adsorbed bilayer graphene, the energy of an isolated Li atom, and the energy of the bilayer graphene, respectively. For an AB-stacked bilayer graphene, we find that the adsorption energies of Li at T-sites and M-sites are −1.36 eV and −2.15 eV, with the E_{ad} of the Li adatom being 1.73 Å and 1.92 Å away from the corresponding hexagon centers, respectively, as listed in Table 1.

Table 1. Computed Adsorption Energies at Different Sites

T-site	E_{ad} (eV)	M-site	E_{ad} (eV)
1	−2.26	1	−2.60
2	−2.00	2	−2.53
3	−1.86	3	−2.47
4	−1.86	4	−2.34
5	−1.98	5	−2.54
6	−2.09	H_m[a]	−2.15
H_t[b]	−1.36		

[a]H_m denotes the hollow sites between two graphene sheets in a pristine AB-stacked bilayer graphene. [b]H_t denotes the hollow sites on the outer surface of a pristine AB-stacked bilayer graphene.

Locally at the defect, the interactions between Li and C atoms are however necessarily different from the case of a pristine bilayer graphene. Figure 2 shows the positions of a subset of the equilibrium Li adsorption sites identified in the vicinity of the Wigner V_2^2 defect, showing six nonidentical T-sites and five M-sites that correspond to local energy minimums. These T-sites and M-sites are numbered from 1−6 and 1−5, respectively. Figure 2 shows us that, among the T-sites, site 1 is centered directly above the defect, and sites 2−5 sit roughly on top of hexagons, and site 6 sits above a pentagon; whereas for the M-sites, site 1 sits above a pentagon and the rest remain on top of hexagons with respect to the bottom sheet. These sites also present the "*basis*" set, from which other equivalent adsorption sites around the defect can be identified via symmetry operations. The corresponding adsorption energies of Li at those sites are listed in Table 1. We note that, for both the T-sites and M-sites, the E_{ad} values of Li at the defect are lower than the ones in a pristine AB stacked bilayer graphene, meaning Li is more energetically favorable around the defect. Thus there is a thermodynamic tendency for intercalated Li atoms to segregate at Wigner defects. To understand the strong binding of Li atoms at the Wigner defect, below we examine the local electronic structure and charge transfer phenomena.

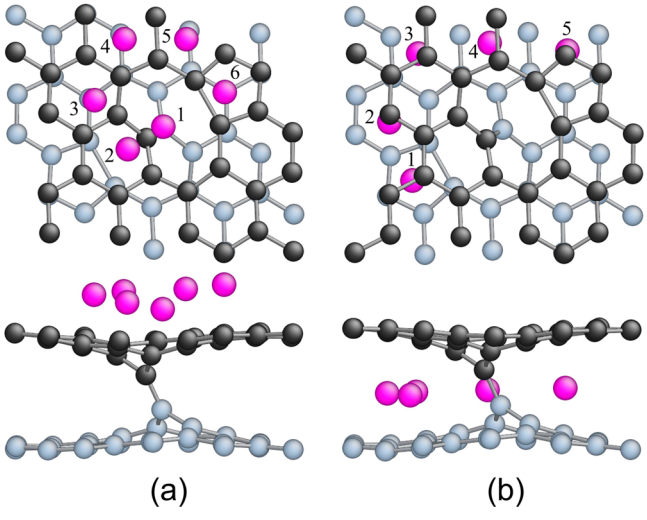

Figure 2. Top and side views of the nonequivalent (a) T-sites 1−6 on graphene surfaces, and (b) M-sites 1−5 between graphene sheets for Li adsorption. Here, the adsorption sites are colored magenta, while the C atoms in different graphene sheets are colored dark gray and cyan, respectively, for clarity.

Figure 3 shows two representative atomic configurations, with Li adsorbed at T-site 1 (cf. Figure 3a) and M-site 1 (cf. Figure 3b), along with the corresponding charge distributions that are represented by the charge density difference $\Delta\rho$, which is defined as

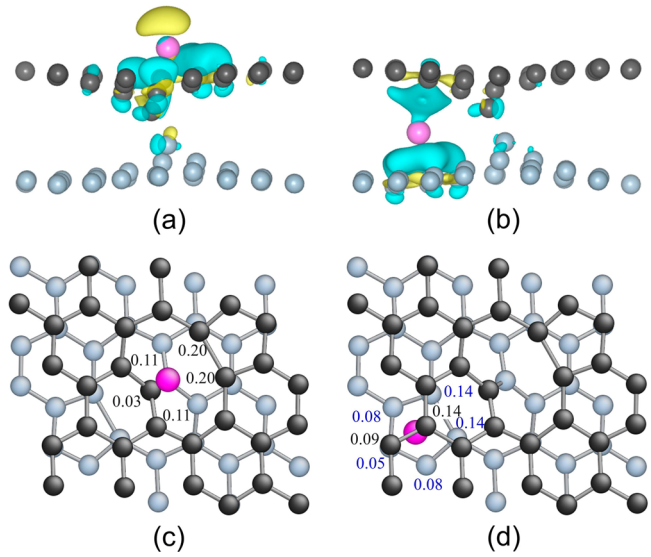

Figure 3. Side views of the charge difference (cf. eq 2) contours around the Wigner V_2^2 defect when a Li atom is adsorbed (a) at T-site 1 and (b) M-site 1, where the Li atom is colored magenta whereas C atoms in the top and bottom graphene sheets are colored dark gray and cyan, respectively. The amounts of charge transfer in the unit of electron from the Li atom to the C atoms neighboring it are indicated in the corresponding top projection views (panels (c) and (d)). The black and blue numbers indicate charge transferred to C atoms on the top and bottom sheets, respectively.

$$\Delta\rho = \rho_{Li+GP} - [\rho_{Li} + \rho_{GP}] \quad (2)$$

where ρ_{Li+GP}, ρ_{Li} and ρ_{GP} denote the charge densities for the entire system, an isolated Li atom, and the defective bilayer graphene, respectively. The $\Delta\rho$ contours are drawn on top of the atomic configurations in Figure 3. In both cases, we see significant charge transfer from the Li atom to its neighboring C atoms. In order to quantify the amount of charge transfer between Li and C atoms, we perform the Barder charge

analysis,[43−45] which computes the estimated charge on each atom. For the particular configuration shown in Figure 3a, where Li occupies T-site 1, the Barder analysis shows a total charge of 2.1 electrons on Li, suggesting Li very much completely lose its valence electron. The charge Li loses is then found to distribute mostly among its immediate C neighbors, as shown in Figure 3c, where the amount of charge transferred to each C atom is indicated. Similar analysis has been performed for the case of Li occupying M-site 1. We again found that the Li atom gives away its valence electron, distributed among its immediate C neighbors. However, in the case of Li being at the M-site 1, charge gets transferred to C atoms in both graphene sheets. We note that, in both cases shown in Figures 3a and 3b, the distribution of charge is largely nonuniform among C atoms neighboring Li, in sharp contrast to the case of Li sitting on a pristine (bilayer) graphene where the transferred charge is mostly distributed uniformly among the six C atoms immediately surrounding Li.[46]

Meanwhile, the corresponding band structures and DOSs of Li-defect systems are computed. Figure 4 shows the results for

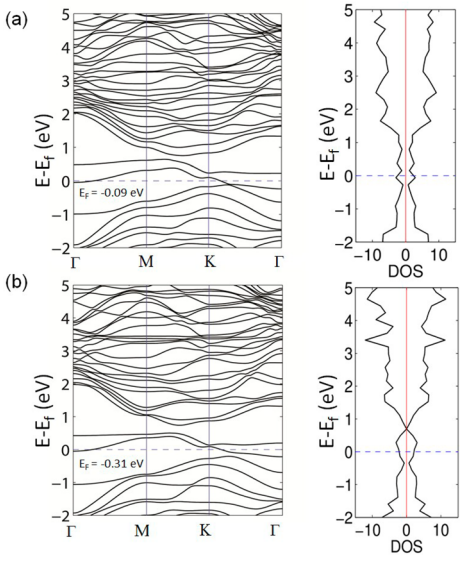

Figure 4. Plots of band structure (left) and density of states (DOS) (right) of the Li-defect systems where a Li atom is adsorbed at (a) T-site 1 and (b) M-site 1, respectively.

the two sample configurations previously shown in Figures 3a and 3b. We see that the Fermi energies are −0.0872 eV (at the T-site) and −3.072 eV (at the M-site), respectively; both are higher than that of a Li-free Wigner V_2^2 defect. In addition, we observe that several bands above the Fermi level shift downward upon Li adsorption, accompanying the disappearance of the band gap, suggesting that the material changes from a semiconductor to a conductor. Similar trends are also observed for Li adsorbed at other locations. These findings resonate with the case of Li adsorption on pristine (bilayer) graphene where zero band gaps and increases in the Fermi energies are also observed. However, we note that the change in the Fermi level induced by Li adsorption at the defect is much smaller.[41,47,48]

2.3. Migration Properties of Li at a Wigner V_2^2 Defect.

Above, we have demonstrated that Li atoms exhibit lower adsorption energies (cf. Table 1) at the Wigner defect. This is likely due to the defect modifying the local charge distribution/electronic structure and, subsequently, Li−C interactions.[41,49] The preferential binding suggests segregation and potential trapping of Li at the defect. This necessarily impacts the local Li kinetics and subsequently battery charging behaviors. For example, the Wigner defect may serve as a potential sink to trap Li motions, which can result in advocate effects in battery capacity and charging/discharging rates. In this regard, we investigate the migration properties of Li at the Wigner defect. From Table 1, we note that Li has the lowest adsorption energies at T-site 1 and M-site 1 (i.e., when adsorbed on outer graphene surface and in the middle, respectively). Thus, they represent the strongest trapping sites at the defect. In the following discussion, we examine the migration of Li from those sites to other equilibrium binding sites in their immediate neighborhoods. The minimum energy paths (MEPs) are examined through NEB calculations with T-site 1 or M-site 1 taken as the initial point and its immediate neighboring binding sites taken as final points. Depending on the distance between the initial and final points, 5−10 images are used in the NEB calculation. The corresponding migration barriers (denoted as E_m) obtained are listed in Table 2, and two representative MEPs are shown in Figure 5.

For Li kinetics starting from T-site 1, the final point can be T-sites 2−6. Among the MEPs, we find that the saddle point occurs on top of a C atom for Li migrating toward T-sites 2−3, and at a bridge site above the C−C bond for Li migrating toward T-sites 4−6. The corresponding E_m ranges from 0.26 eV to 0.54 eV (cf. Table 2). We note that these E_m values are on the same order as the E_m (i.e., spanning from 0.322 to 0.34 eV) of Li on the outer surface of a graphene or graphite,[50,51] although, on average, higher. Also we note that the MEP for Li migration from T-site 1 → T-site 2 yields an E_m of 0.26 eV, suggesting that Li can easily escape from the Wigner defect through that path.

Table 2. The Migration Barrier (E_m) of Li

T-site Data					
path	T-site 1→2	T-site 1→3	T-site 1→4	T-site 1→5	T-site 1→6
E_m (eV)	0.260	0.480	0.540	0.498	0.436
AB-Stacked Bilayer Graphene Data					
path	adjacent sites on surface of AB-stacked bilayer graphene				
E_m (eV)	0.33,[a] 0.322,[b] and 0.34[c]				
M-site Data					
path	M-site 1→I5				
E_m (eV)	0.083				

[a]Data obtained from this work. [b]Data taken from ref 50. [c]Data taken from ref 46.

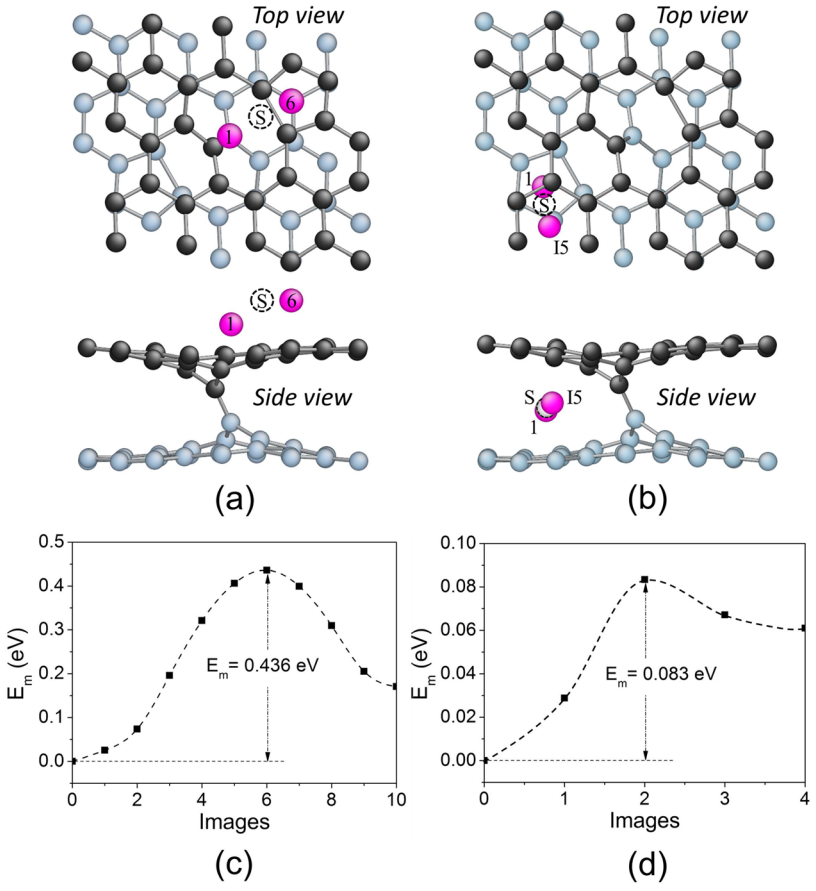

Figure 5. Migration paths of Li (identified via the NEB calculations) (a) from T-site 1 to T-site 6 and (b) from M-site 1 to its neighboring image site I5, with the Li positions corresponding to the saddle points indicated by the dashed white circles. The corresponding MEPs are shown in panels (c) and (d), respectively.

On the other hand, for interlayer Li kinetics at the Wigner defect, the migration does not occur directly between the M-sites identified. Instead, a MEP starting from a M-site would end at an image M-site. Those image M-sites are a set of Li adsorption sites that are equivalent images of the M-sites listed in Table 1 due to the *Ci* (i.e., inverse) symmetry of the Wigner V_2^2 defect.[52] For instance, the MEP starts from the M-site 1 would end at a site (denoted as site I5 in Figure 5) that is an equivalent image of the M-site 5, as illustrated in Figures 5b and 5d. Overall, our findings indicate that the E_m value between M-sites (and image M-sites) at the Wigner defect is on the order of 0.08 eV (e.g., E_m = 0.083 eV for migration from M-site 1 to image M-site I5, cf. Figures 5b and 5d), significantly lower than the migration barrier for Li motions on the outer graphene surface. This value of E_m is also lower than the interlayer Li migration barrier in graphite (~0.2 eV).[53] The low E_m presumably comes from the reduced interlayer separation and AB-stacking locally at the defect. In addition, the presence of the image M-sites effectively doubles the Li adsorption sites and, thus, the charge capacity compared to the normal Li-graphite system. We note, however, that Li intercalation will induce the overall sequence of graphene sheets to change from AB-stacking to AA-stacking.[7] Thus, a competition between the stacking sequences is expected during lithiation. Nevertheless, the atomic configuration in the immediate vicinity of the Wigner defect likely can be (partially) retained, because of the strong interlayer covalent bonding.

From our results on Li migration, we note that, while the Wigner V_2^2 defect has some adverse effects on Li migration on the graphene surfaces (cf. Table 2), it facilitates Li diffusion and increases local charge capacity for interlayer Li intercalation, because of the defect-induced stacking sequence and reduction in interlayer spacing. In addition, it was postulated by several studies[37,54,55] that structural defects, particularly vacancy-like defects, can aid Li diffusion through graphene sheets. Although the through-layer Li kinetics is beyond the scope of our current study, we have performed some preliminary calculations that show the diffusion barrier for through-layer Li diffusion via the Wigner defect is 7−8 eV, being 2−3 eV smaller than the diffusion through a pristine graphene sheet.[37] Thus, the effects of the Wigner defect are 2-fold. Given that the overall Li kinetics is a combination of contributions from surface, interlayer and through-layer Li diffusion, one may tune the defect density together with the surface-to-volume ratio to optimize the performance of 3D graphene scaffolds in Li-ion batteries.

3. CONCLUSIONS

To conclude, we have performed first-principles calculations to study the adsorption energetics and transport kinetics of Li in the vicinity of a Wigner V_2^2 defect to illustrate the interplay between Li atoms and irradiation-induced defects in graphite/multilayer graphene. We have identified equilibrium adsorption sites for Li at the Wigner defect and shown that they are energetically preferable, compared to the sites on pristine

(bilayer) graphene. We find that the migration barriers for Li diffusion on the graphene surface increase at the vicinity of the defect, suggesting adverse effects of defects on surface Li motions. On the other hand, the interlayer Li diffusion along with the charge capacity are enhanced around the defect, because of the reduced interlayer spacing and particular symmetry associated with the defect. Our study provides important insights toward the design and application of irradiation-defects hybridized graphene scaffolds in Li-ion batteries.

■ ASSOCIATED CONTENT

Supporting Information

This material is available free of charge via the Internet at http://pubs.acs.org.

■ AUTHOR INFORMATION

Corresponding Authors

*E-mail: jun.song2@mcgill.ca (J.S.).
*E-mail: nikhil.medhekar@monash.edu (N.V.M.).

Notes

The authors declare no competing financial interest.

■ ACKNOWLEDGMENTS

The authors acknowledge support of this work by the NSERC Discovery grant (No. RGPIN 418469-2012). The authors also would like to acknowledge Supercomputer Consortium Laval UQAM McGill and Eastern Quebec, as well as MASSIVE and NCI computing infrastructure provided by the Australian Government, for providing computing power.

■ REFERENCES

(1) Dresselhaus, M. S.; Dresselhaus, G. *Adv. Phys.* **1981**, *30*, 139−326.
(2) Pistolia, G. *Lithium Batteries: New Materials, Developments, and Perspectives*; Elsevier: New York, 1994.
(3) Dahn, J. R.; Zheng, T.; Liu, Y. H.; Xue, J. S. *Science* **1995**, *270*, 590−593.
(4) Fischer, J. E. *Chem. Innovation* **2000**, *30*, 21−27.
(5) Juza, R.; Wehle, V. *Naturwissenschaften* **1965**, *52*, 560.
(6) Kaskhedikar, N. A.; Maier, J. *Adv. Mater.* **2009**, *21*, 2664−2680.
(7) Winter, M.; Besenhard, J. O.; Spahr, M. E.; Novak, P. *Adv. Mater.* **1998**, *10*, 725−763.
(8) Kasuh, T.; Mabuchi, A.; Tokumitsu, K.; Fujimoto, H. *J. Power Sources* **1997**, *68*, 99−101.
(9) Azuma, H.; Imoto, H.; Yamada, S.; Sekai, K. *J. Power Sources* **1999**, *82*, 1−7.
(10) Tokumitsu, K.; Fujimoto, H.; Mabuchi, A.; Kasuh, T. *Carbon* **1999**, *37*, 1599−1605.
(11) Castro Neto, A. H.; Guinea, F.; Peres, N. M. R.; Novoselov, K. S.; Geim, A. K. *Rev. Mod. Phys.* **2009**, *81*, 109−162.
(12) Geim, A. K.; Novoselov, K. S. *Nat. Mater.* **2007**, *6*, 183−191.
(13) Balandin, A. A.; Ghosh, S.; Bao, W. Z.; Calizo, I.; Teweldebrhan, D.; Miao, F.; Lau, C. N. *Nano Lett.* **2008**, *8*, 902−907.
(14) Evanoff, K.; Magasinski, A.; Yang, J. B.; Yushin, G. *Adv. Energy Mater.* **2011**, *1*, 495−498.
(15) Magasinski, A.; Dixon, P.; Hertzberg, B.; Kvit, A.; Ayala, J.; Yushin, G. *Nat. Mater.* **2010**, *9*, 353−358.
(16) Lung, H.; Hu, B.; Wu, F.-Y.; Lin, C.-T.; Khlobystov, A. N.; Li, L.-J. *Nat. Commun.* **2013**, *4*, 1687−1693.
(17) Boukamp, B. A.; Lesh, G. C.; Huggins, R. A. *J. Electrochem. Soc.* **1981**, *128*, 725−729.
(18) Huggins, R. A. *J. Power Sources* **1999**, *81*, 13−19.
(19) Balbuena, P. B.; Wang, Y. *Lithium-Ion Batteries: Solid-Electrolyte Interphase*; Imperial College Press: London, 2004.
(20) Peled, E. *J. Electrochem. Soc.* **1979**, *126*, 2047−2051.
(21) Aurbach, D.; Markovsky, B.; Weissman, I.; Levi, E.; Ein-Eli, Y. *Electrochim. Acta* **1999**, *45*, 67−86.
(22) Gnanaraj, J. S.; Levi, M. D.; Levi, E.; Salitra, G.; Aurbach, D.; Fischer, J. E.; Claye, A. *J. Electrochem. Soc.* **2001**, *148*, A525−A536.
(23) da Silva, A. J. R.; Fazzio, A.; Antonelli, A. *Nano Lett.* **2005**, *5*, 1045−1049.
(24) Banhart, F. *Rep. Prog. Phys.* **1999**, *62*, 1181−1221.
(25) Kis, A.; Csanyi, G.; Salvetat, J. P.; Lee, T. N.; Couteau, E.; Kulik, A. J.; Benoit, W.; Brugger, J.; Forro, L. *Nat. Mater.* **2004**, *3*, 153−157.
(26) Peng, B.; Locascio, M.; Zapol, P.; Li, S. Y.; Mielke, S. L.; Schatz, G. C.; Espinosa, H. D. *Nat. Nanotechnol.* **2008**, *3*, 626−631.
(27) Sammalkorpi, M.; Krasheninnikov, A.; Kuronen, A.; Nordlund, K.; Kaski, K. *Phys. Rev. B* **2004**, *70*, 245416.
(28) Huhtala, M.; Krasheninnikov, A. V.; Aittoniemi, J.; Stuart, S. J.; Nordlund, K.; Kaski, K. *Phys. Rev. B* **2004**, *70*, 045404.
(29) Iwata, T. *J. Nucl. Mater.* **1985**, *133*, 361−364.
(30) Kelly, B. T. *The Physics of Graphite*; Applied Science: London, 1981.
(31) Kelly, B. T.; Marsden, B. J.; Hall, K. *Irradiation Damage in Graphite due to Fast Neutrons in Fission and Fusion Systems*; International Atomic Energy Agency, No. IAEA-TECDOC-1154, September 2000.
(32) Telling, R. H.; Ewels, C. P.; El-Barbary, A. A.; Heggie, M. I. *Nat. Mater.* **2003**, *2*, 333−337.
(33) Kresse, G.; Furthmuller, J. *Comput. Mater. Sci.* **1996**, *6*, 15−50.
(34) Kresse, G.; Joubert, D. *Phys. Rev. B* **1999**, *59*, 1758−1775.
(35) Blochl, P. E.; Jepsen, O.; Andersen, O. K. *Phys. Rev. B* **1994**, *49*, 16223−16233.
(36) Henkelman, G.; Jonsson, H. *J. Chem. Phys.* **2000**, *113*, 9978−9985.
(37) Yao, F.; Gunes, F.; Ta, H. Q.; Lee, S. M.; Chae, S. J.; Sheem, K. Y.; Cojocaru, C. S.; Xie, S. S.; Lee, Y. H. *J. Am. Chem. Soc.* **2012**, *134*, 8646−8654.
(38) Fan, X. F.; Zheng, W. T.; Kuo, J. L.; Singh, D. J. *ACS Appl. Mater. Interfaces* **2013**, *5*, 7793−7797.
(39) Note that the defect-induced band gap, however, will disappear in the dilute limit and the presence of a defect will show up as a doping level instead.
(40) Garay-Tapia, A. M.; Romero, A. H.; Barone, V. *J. Chem. Theory Comput.* **2012**, *8*, 1064−1071.
(41) Fan, X. F.; Zheng, W. T.; Kuo, J. L. *ACS Appl. Mater. Interfaces* **2012**, *4*, 2432−2438.
(42) Note that, therefore, for an AB stacking bi-layer graphene, there would be twice as many M-sites as there are T-sites.
(43) Sanville, E.; Kenny, S. D.; Smith, R.; Henkelman, G. *J. Comput. Chem.* **2007**, *28*, 899−908.
(44) Henkelman, G.; Arnaldsson, A.; Jonsson, H. *Comput. Mater. Sci.* **2006**, *36*, 354−360.
(45) Tang, W.; Sanville, E.; Henkelman, G. *J. Phys.: Condens. Matter* **2009**, *21*, 084204.
(46) Valencia, F.; Romero, A. H.; Ancilotto, F.; Silvestrelli, P. L. *J. Phys. Chem. B* **2006**, *110*, 14832−14841.
(47) Chan, K. T.; Neaton, J. B.; Cohen, M. L. *Phys. Rev. B* **2008**, *77*, 235430.
(48) Note that, for Li adsorption on pristine graphene or bilayer graphene, the upshift in the Fermi energy is ∼1 eV.
(49) Zhou, L. J.; Hou, Z. F.; Wu, L. M. *J. Phys. Chem. C* **2012**, *116*, 21780−21787.
(50) Kubota, Y.; Ozawa, N.; Nakanishi, H.; Kasai, H. *J. Phys. Soc. Jpn.* **2010**, *79*, 014601.
(51) Chan, K. T.; Neaton, J. B.; Cohen, M. L. *Phys. Rev. B* **2008**, *77*, 235430.
(52) Note that those image sites are equivalently M-sites, with respect to the top graphene sheet.
(53) Toyoura, K.; Koyama, Y.; Kuwabara, A.; Oba, F.; Tanaka, I. *Phys. Rev. B* **2008**, *78*, 214303.
(54) Tran, T.; Kinoshita, K. *J. Electroanal. Chem.* **1995**, *386*, 221−224.

(55) Persson, K.; Sethuraman, V. A.; Hardwick, L. J.; Hinuma, Y.; Meng, Y. S.; van der Ven, A.; Srinivasan, V.; Kostecki, R.; Ceder, G. *J. Phys. Chem. Lett.* **2010**, *1*, 1176−1180.